Composites Research

Vol. 32, No. 5, 249-257 (2019)
DOI: http://dx.doi.org/10.7234/composres.2019.32.5.249
ISSN 2288-2103(Print), ISSN 2288-2111(Online)

Paper

Test and Analysis of Triaxially Braided Composite Circular Arch under Three-Point Bending

Biruk F. Nega*, Kyeongsik Woo†, Hansol Lee*****

ABSTRACT: In this paper, the buckling behavior of triaxially braided circular arch with monosymmetric open section subjected to three-point bending was studied experimentally and numerically. First, test specimens were manufactured using vacuum assisted resin transfer molding (VARTM). Then the specimen was tested under three-point bending to determine the ultimate buckling strength. Before performing the numerical analysis, effective material properties of the braided composite were obtained through micro-meso scale analysis virtual testing validated with available test results. Then linear buckling analysis and geometrically non-linear post buckling analysis, established to simulate the test setup, were performed to study the buckling behavior of the composite frame. Analysis results were compared with experimentally obtained ones for verification. The effect of manufacturing defects of tow misalignment, irregular surface and resin rich region, and uncertainties during test setup were studied using numerical models. From the numerical analyses performed it was observed that both manufacturing defect and uncertainties had effect on the buckling behavior and strength.

Key Words: Triaxial braid, Composite arch frame, Buckling, Manufacturing defect

1. INTRODUCTION

In recent years advanced composite materials are being extensively used as primary structures in aerospace, military and automotive industries. They are favored for their high strength to weight ratio, corrosion resistance, requirement in material anisotropy and the advantage that their properties can be tailored to yield specific requirements. As laminated composite materials have been used in layered stacking the propensity to delamination due to out-of-plane loading was high [1] which is due to relatively poor resin strength which held the fibers together. Hence braided textile composites which are manufactured by interweaving tows running in different direction were developed to lessen delamination due to out-of-plane loading. Braided textile composites are favored over pre-preg laminates for their better out-of-plane properties, near net shape fabrication, impact and delamination resistance and overall high performance [2]. They are widely used in various application areas including thin walled composite structures.

Thin walled composite structures are commonly used in aerospace industries due to sufficient in-plane performance at the same time reducing the overall structural weight [3]. One area where thin walled composites are employed is arched frames. Composite arched frames offer combined advantage of high strength-to-weight ratio and efficient load transferring mechanism through both axial compression in the hoop direction and bending action which make them suit for many applications. The distinguishing characteristic of arches from beams is that the presence of end reaction force as they transfer the loading into axial compression in addition to the considerable rise of the axis at the center. For beams supporting transverse loading the bending moment increases as the length and become uneconomical for longer span structures or structural members, hence arched structures are favored for such applications.

Consequently, arched structures offer advantage as they

Received 15 May 2019, received in revised form 5 October 2019, accepted 10 October 2019

*Dept. of Civil Systems Engineering, Chungbuk National University
**†School of Civil Engineering, Chungbuk National University, Corresponding author (E-mail: kw3235@chungbuk.ac.kr)
***Nexcoms, Co., Ltd.

develop horizontal reaction force which reduces the design bending moment [4]. And on the contrary, the component of the end reaction in arched beams will also be the cause of buckling and the structure may fail due to torsional buckling. Hence the performance of arched structure to flexural torsional buckling depend on the combination of in-plane and out-of-plane deflections, rotations, and twist and warping of the cross section [5]. The buckling resistance of arched structures in general depends on factors such as slenderness, rise-to-span ratios, out-of-plane bending and torsional rigidities, arch-end restraints and initial geometric imperfections. Moreover, circular frames having open cross section, i.e., mono-symmetric cross sections such as C channels, are subjected to severe instability issue. This is due to the development of additional torsional and twisting behavior as the shear center do not coincide with center of gravity of the cross section.

Previous studies to investigate the lateral torsional buckling of arched structures were mainly focused on steel sections. For instance, Guo *et al.* [6] studied the out-of-plane inelastic buckling strength of steel arches under symmetric and non-symmetric loading conditions using experimental test and finite element method. From their study they found out that the inelastic buckling strength of fixed arch steel structures is influenced significantly by the magnitude and distribution of initial out-of-plane geometric imperfection. Another study by Dou *et al.* [5] investigated the flexural-torsional ultimate resistance of steel arches under symmetric and unsymmetrical loading using experimental test and finite element techniques. Following the development of industries in using advanced composite materials for thin walled structures, studies are being performed on lateral torsional behavior of composite members too.

For instance, Barbero and Tomblin [7] investigated global buckling and determined critical buckling load of fiber reinforced composite I-beam using experimental tests and compared with theoretical predictions. Davalos *et al.* [8] also performed combined analytical and experimental study on the flexural torsional buckling of pultruded FRP composite. Another study conducted by Omidvar and Ghorbanpoor [9] developed non-linear finite element (NLFE) analysis based on lagrangian formulation for the analysis of thin-walled open section composite structural member.

In the current study buckling behavior of triaxially braided composite arch frame was studied using both experimental test and finite element analysis. Elastic mechanical properties were first obtained using micro-meso multi-scale finite element analysis from constituent material properties and measured braid geometric dimensions. Then linear buckling analysis and geometrically non-linear post buckling analysis were performed to study the buckling behavior and subsequently determine the ultimate buckling load. Finally, the effect of defects and uncertainties were studied using numerical model.

2. EXPERIMENT

For the current study, the test specimens were manufactured from high performance carbon fibers impregnated with epoxy matrix. The axial tow is made from 37-800WD 30K high performance carbon (made by Mitsubishi Rayon Carbon Fiber & Composites, Inc.) and the bias tow from TR50S-12 fiber (made by Grafil Inc.). Fig. 1 shows the specimen preparation. First, triaxial braid preform sheets were fabricated, which were then stacked and molded with rigid steel blocks using VaRTM (Vacuum Assisted Resin Transfer Molding) composite manufacturing process which uses vacuum assisted resin transfer into braided fiber lay-ups. After impregnation the composite frame was allowed to cure at specified temperature. The braiding angle and the fiber volume fraction of (f_{vT}) were measured to be 66° and 47%, respectively. The constituent fiber and matrix properties are given in Table 1.

The finished product was manufactured with the required outer cross-sectional dimensions and diameter with an average thickness of 2.57 mm. The circular frame which had a diameter D = 2569.4 mm was then cut in to test sample

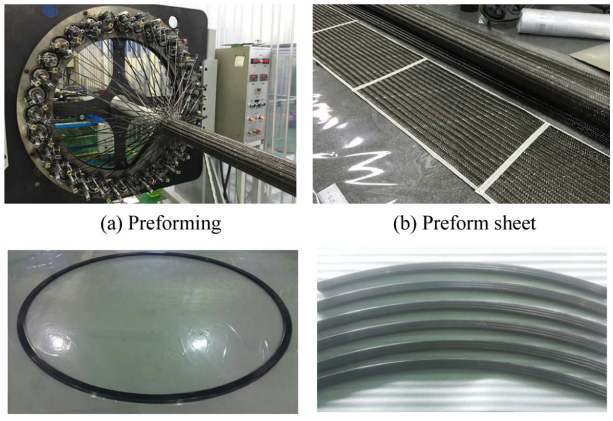

(a) Preforming (b) Preform sheet

(c) Manufactured channel section (b) Cut test specimens

Fig. 1. Specimen preparation

Table 1. Constituent material properties

	Axial tow (37-800WD)	Bias tow (TR50S-12L)	Matrix
E_{11} (GPa)	255	240	2.9
E_{22} (GPa)	34	32	-
G_{12} (GPa)	24.2	23	1.04
G_{23} (GPa)	12.6	11.9	-
ν_{12}	0.23	0.22	0.39
ν_{23}	0.36	0.34	-
X_T (MPa)	5490	2620	74.3
X_C (MPa)	4900	2532	101.4
S (MPa)	-	-	135.84

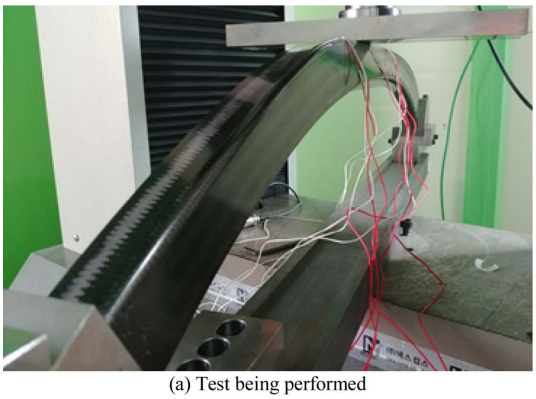

(a) Test being performed

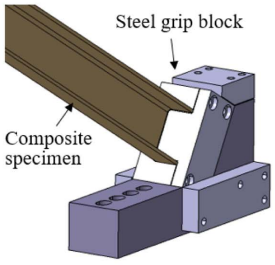

(b) Grip block

Fig. 2. Specimen under test

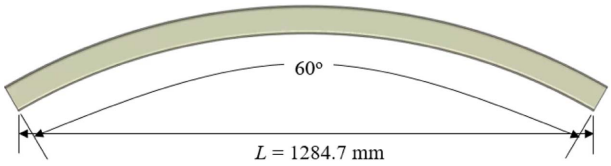

(a) Global dimensions of tested specimen

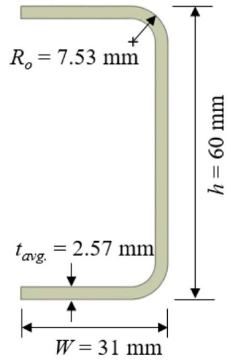

(b) Channel cross-section

Fig. 3. Configuration of composite circular arch

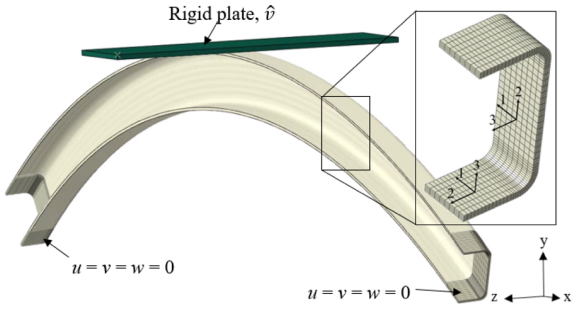

Fig. 4. FE modeling of composite arch

dimension with 1/6 (60°) circular axis as shown in Fig. 1(d). The detail cross-sectional dimension of the test specimen is given in the next section.

Fig. 2 shows the test being performed, where the two ends of the composite frame were constrained by a steel grip block system. One of the two grip blocks is shown Fig. 2(b) which is assembled to the bottom steel bar by bolts. The vertical loading was applied at the crown via a thick steel plate. The test was performed using a universal testing machine (UTM) in accordance with standard guideline [10] with displacement-controlled loading. The speed of the applied displacement was 1 mm/min. The vertical loading and the corresponding specimen displacement were measured from attached load cell and movement of the cross head, respectively. Local strain responses were also read from strain gauges attached at different locations.

3. ANALYSIS

3.1 Finite element modeling of circular arch

Fig. 3 shows analysis configuration with its global and cross-sectional dimensions for pristine composite circular arch structure. The specimen had a length of L = 1224.7 mm between inner support ends with cross sectional dimension of height h = 60 mm, width W = 31 mm and outer curve radius R_o = 7.53 mm.

Fig. 4 shows the finite element model with its boundary conditions. For the analysis of circular arch, commercial software ABAQUS was adopted to establish finite element simulation model of the test process with geometrically non-linear static analysis procedure. Even though shell and continuum shell elements are commonly used in finite element modeling of thin walled structures, 3D solid elements were used in the current study to consider thickness-wise imperfections which will be discussed later.

After preliminary mesh convergence study, the composite circular arch was modeled using 135,408 eight node solid elements (C3D8) and 171,825 nodes for specimen without manufacturing defect, and other configurations were also meshed with the same or higher refinement. The element size was determined to explicitly model the thickness variation occurred at the inner surface in the pattern of braided fiber tows. It was also observed refined local mesh refinement on upper curved section is important to ensure smooth contact transfer between the loading plate and specimen during deformation. As in the actual test the loading was introduced by means of flat plate; an analytically rigid plate was used with displacement-controlled loading. Surface-to-surface contact having normal and tangential properties was defined between the steel plate

and composite circular arch with 0.2 friction coefficient. Orthotropic material orientation was assigned discretely where material direction 1 is in the axis of the arch, 2 in transverse direction and 3 in the out-of-plane direction at every point.

3.2 Buckling analysis

In long and thin composite members subjected to compressive loading, buckling failure occurs locally or globally before any other types of material or instability failure [11]. Likewise, in long composite members with non-symmetric cross-section there exist additional coupled bending and torsion [12], hence, their flexural torsional buckling should be considered.

The buckling analysis using finite element analysis could be performed in two ways: linear buckling analysis and non-linear post-buckling analysis. Linear buckling analysis is commonly performed to obtain the theoretical buckling load and the corresponding buckling mode shapes. But in actual structures, imperfections and non-linearities resulting from material and geometry prevent from achieving the theoretical elastic buckling strength. In contrast, non-linear post-buckling analyses are performed to get detailed information on the progressive deformation, strain and stress states and also on how the structure behaves after initiation of buckling. To instigate buckling one may introduce initial geometric imperfection to finite element mesh. The imperfection can obtained by directly measuring the magnitude and distribution of the imperfection in structure using ultrasonic scan [13], total station instrument [5] or other suitable mechanisms. Other alternatives to instigate buckling are applying small perturbation load [14], introducing random imperfection by disturbing nodal coordinates [15] or imperfection based on preceding linear buckling analysis [16].

While structures with symmetric geometry and loading condition require buckling instigation techniques, buckling occurs without the instigation techniques for mono-symmetric cross sections, as in the current study. This is due to the non-coincident nature of shear center and centroid of open cross sections where the reaction shear flow causes twisting which in turn instigates buckling. Hence linear and geometrically nonlinear buckling analyses were performed without such buckling instigation strategies. It was found from a preliminary analysis that no material failure occurred because all stresses were lower than the material strengths, and therefore failure modeling was not included.

3.3 Material properties

For the triaxially braided textile composite used in this study, uniaxial tensile tests in the material 1- and 2-directions were performed to obtain elastic properties [17] according to specific ASTM D3039 standard testing procedures [18]. For material properties for which tests were not performed, micro-meso multi-scale finite element analysis was performed using measured geometric braiding parameters. First, micro-scale analyses were performed to obtain homogenized tow properties from constituent material properties given in Table 1. For the micro-scale analysis, commercial software MCQ/Composites [19] was used with the fiber volume fraction in the tow (v_f^{tow}) of 84.3%. Next, the effective lamina properties were obtained through meso-scale unit cell analyses simulating 3 uniaxial tension and 3 shear tests with the braiding angle of 66° and the total fiber volume fraction (v_{fT}) of 47%.

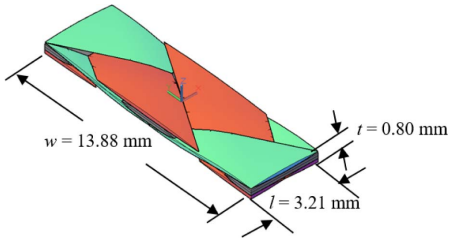

Fig. 5. Meso-scale unit cell of triaxial braid composite

Table 2. Elastic properties of triaxial braid composite

E_{11}	E_{22}	E_{33}	ν_{12}	ν_{13}	ν_{23}	G_{12}	G_{13}	G_{23}
49.2	46.7	9.74	0.21	0.39	0.47	10.1	2.43	2.60

(Unit of modulus = GPa)

For the meso-scale unit cell analysis, a repeating meso-scale unit cell model was generated as shown in Fig. 5 from measured dimensions of the triaxially braided test specimen. The geometry was generated assuming both axial and bias tow cross-section to be lenticular and to run over straight and undulating path for axial and bias tow, respectively. (Detail description of the modeling process can be found in Ref. [20].) With the generated finite element unit cell model, effective material properties were obtained by performing a series of virtual tests simulating uniaxial and shear tests in different directions. Table 2 summarizes the material properties obtained by tests and numerical analyses. The predicted results agreed well to the test results [11] which validated the numerical approach.

3.4 Defect identification

The test specimen was examined and found to have a number of manufacturing defects. These include tow misalignment, resin rich region, cross-sectional thickness variation, and irregular cross-section. The effect of these defects was investigated modeling them numerically.

Fig. 6 shows the irregular inner surface and resin rich defects. Cross-sectional dimensions measurements at different locations revealed different thickness value at the web, upper flange and bottom flange. Stochastic distribution of this variation was measured at 32 different locations at equal intervals which showed the average thicknesses of 2.34 mm, 2.79 mm, and 2.56 mm for the upper and lower flange, and for the web,

respectively, with the standard deviation of 0.297. In addition to the average thickness variation, the manufacturing process made the inner face (vacuum bag side) of the specimen wavy according to the microstructural shape of axial and bias tows with 0.1 mm amplitude while the outer surface (tool side) was flat. Also, during molding, as the braided mat was laid on steel mold, the impregnated resin near the curve was squeezed out to the re-entrant corner of the inner face. These defects of irregular inner surface and resin rich region in the manufacturing process are taken into account in the numerical modeling, see Fig. 6.

Similarly, the tow misalignment was measured from the test specimen. The misalignment occurred at 25 locations with the average off-set from the center line of 2.5°. The misalignment

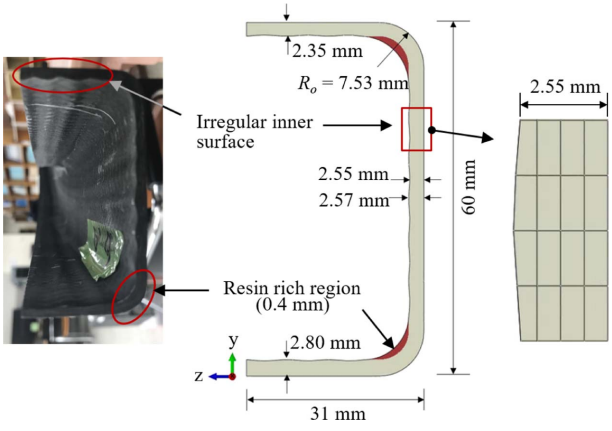

Fig. 6. Defect of irregular inner surface and resin rich region

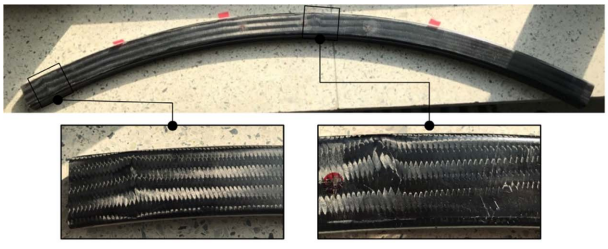

(a) Measurement of tow misalignment in the test sample

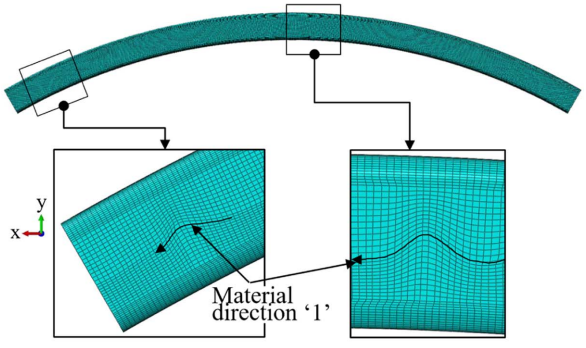

(b) Modeling tow misalignment in numerical model

Fig. 7. Measurement and modeling of tow misalignment

was explicitly considered by first calculating the effective properties for the misaligned part [17] and then by arranging the mesh shape to follow the misaligned axial tow direction. In Fig. 7, the typical tow misalignment and their corresponding finite element modeling are shown. The material's fiber direction was defined by connecting measured offsets at different location with spline curve.

During mounting the specimen for test, due to imperfect support grip and specimen placement around 3° specimen tilting was measured from the span center to the crown and vertical axis. This loading imperfection was taken into account in the finite element modeling.

4. RESULTS AND DISCUSSION

4.1 Linear buckling analysis

Fig. 8 and Table 3 show the first nine buckling mode shapes and the first ten buckling loads, respectively, from linear eigenvalue analysis with their corresponding scale factors. The analysis was performed by applying a vertical load along the line at the upper surface which was the initial line contact between the specimen and the loading plate throughout the analysis. With regard to computational resource continuum shell can be more effective in the analysis of thin-walled structures as fewer elements are used. However, the continuum shell modeling has limitation in modeling of the present structure because the characteristic thickness scale is not so small and the section definition of the cross-sectional thickness variations as shown in Fig. 6 cannot be achieved. Hence, 3D solid element modeling was used for all analyses.

As can be seen from the figure, the first and the eighth buckling modes are the global modes dominated by the out-of-plane global symmetric and anti-symmetric deformations of

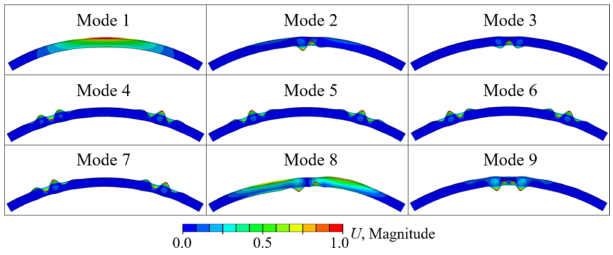

Fig. 8. Linear buckling modes (Disp. scale = 25)

Table 3. Linear buckling load

Mode	P_{cr} (N)	Mode	P_{cr} (N)
1	4771.4	6	9291.9
2	7919.2	7	9292.0
3	7921.2	8	9917.5
4	9291.7	9	10042
5	9291.8	10	10426

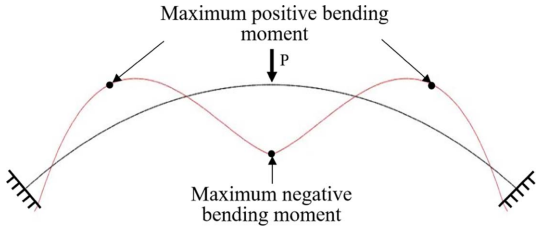

Fig. 9. Typical bending moment distribution of rectangular arch

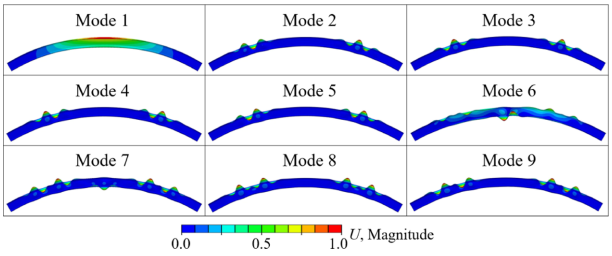

Fig. 10. Buckling mode for cross-sectional defect (Disp. scale = 25)

Table 4. Effect of defects on linear buckling load

Mode	Cross-sectional defect		Tow misalignment	
	P_{cr} (N)	% diff.	P_{cr} (N)	% diff.
1	4592.9	-3.741 (1)	4822.8	1.077
2	7956.2	-14.37 (4)	7952.5	0.420
3	7956.3	-14.37 (5)	7957.6	0.453
4	7956.3	-14.37 (6)	9242.1	-0.534
5	7956.3	-14.37 (7)	9242.7	-0.528
6	8865.7	-10.61 (8)	9278.0	-0.150
7	8872.9	-14.90 (10)	9278.2	-0.149
8	8875.6	-14.88 (11)	9957.7	0.405
9	8875.6	-14.89 (12)	10066	0.239
10	8880.3	-13.85 (13)	10357	-0.662

the specimen respectively, while others are more of localized deformation of bottom flange near the crown or top flange between the crown and the support. On a typical simplified case where the concentrated load applied at the crown of fixed circular arch with rectangular cross section, the maximum bending moment appears at the crown and second pairs, symmetric, between the crown and the support having opposite sign as shown in Fig. 9. Consequently, the locations of local in-plane buckling are in agreement with these locations.

As shown in Fig. 10 and Table 4, the cross sectional defect affected the buckling mode shapes and the buckling loads significantly. While the first mode shape and buckling load agreed with small difference with those of the pristine model, the modes 2-5 of the model with cross-sectional defect matched with the modes 4-6 of the pristine model and there occurred approximately 14% difference in buckling loads. The

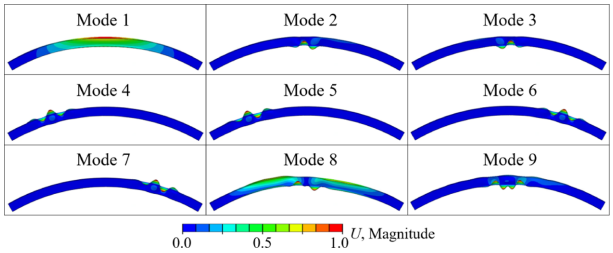

Fig. 11. Buckling modes for tow misalignment (Disp. scale = 25)

sixth mode of the model with the cross sectional defect seemed to match with the eighth mode of the pristine model, but the mode shape was more complicated and the buckling load differed by 10.6% compared to that of the pristine model. Similarly, the modes 7-10 with the cross sectional defect corresponded to the modes 10-13 of the pristine model with approximately 15% differences.

For the case of tow misalignment shown in Fig. 11, the effect was found to be not so significant. The mode shapes of modes 1-3, 8 and 9 matched with those of the pristine model and the difference in the buckling loads was relatively small. For modes 4-7, the buckling deformation developed non-symmetrically only at one side due to the non-symmetric occurrence of the local tow misalignment defects, but the difference in the buckling loads was small. From these results, one can see that the cross sectional defect had a larger influence on the linear buckling behavior than the tow misalignment defect.

4.2 Geometrically nonlinear post-buckling analysis

In the current configuration, even though buckling occurs naturally due to the mono-symmetric cross section, preliminary imperfection sensitivity analysis was also performed with geometrically non-linear post buckling analysis. For this purpose, the lowest fundamental buckling mode from the linear buckling analysis was selected, scaled, and applied to the mesh as initial geometric imperfection. Imperfection magnitude ranges that are commonly used were considered and found to have insignificant effect on both the elastic response and the ultimate buckling load.

First, a three-dimensional geometrically nonlinear analysis was performed for the pristine model. A displacement controlled vertical load was applied by a flat steel plate which transferred to the composite frame structure through contact at the crown part of the frame. Fig. 12 shows the progressive deformation history at three different loading stages marking the local buckling developments. The circled numbers indicate the applied load state shown in the load-displacement curve of Fig. 13. While the linear eigen analysis predicted the first global buckling deformation mode to occur at P_{cr} = 4771.4 N, the non-linear analysis showed the forward bending deformation to occur from the very beginning which can also be seen form the highly non-linear load-displacement curve.

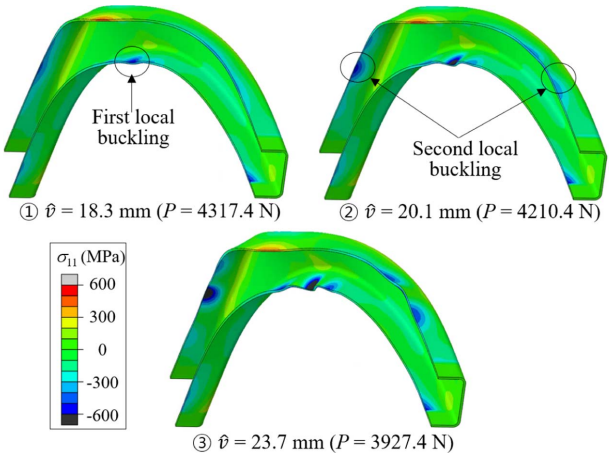

Fig. 12. Predicted deformation history for pristine model

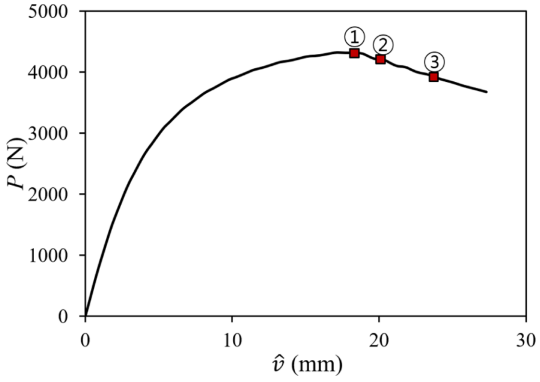

Fig. 13. Predicted load-displacement for pristine model

As the applied load was further increased to point (1), the deformation grows which gave rise to the compressive stress at the bottom flange of the mid-section part of the frame structure. This compressive stress instigated local buckling there and it was this initiation of the local buckling which determined the ultimate buckling load of 4317.4 N. The second and third instability modes predicted from linear eigen analysis were anti-symmetric and symmetric, respectively, at the bottom flange of the crown part, but the nonlinear analysis showed symmetric deformation at the same location, i.e., the second mode was skipped and the third mode developed. After that, the buckling process proceeded quickly and the load-displacement curve started falling.

Then at load point (2), while the local buckling deformation further developed and a pair of local buckling started to appear at the upper flange between the crown and the support. As the loading was further increased in the post-buckling regime, point (3), previously instigated global and local buckling grew in size and the load-displacement curve further decreased.

4.3 Effect of defects

From examination of the test sample and test setup, various imperfections were detected. These include cross sectional defect, local tow misalignment, and specimen tilting. Out of these defects and uncertainties, the specimen tilting had a considerable effect on predicted stiffness and ultimate buckling load. Due to the nature of the test set-up, i.e., imperfect support grip and uncertainties in the specimen set up for test 3° specimen tilting was measured initially when full contact was developed between the loading plate and the specimen. Parametric study for this tilting angle (α) was performed and predicted load-displacement curves and its effect on ultimate buckling load and specimen stiffness are presented in Figs. 14 and 15, respectively. Specimen stiffness or the slope of the load-displacement curve was computed on the initial linear response range. Analyses were performed for tilting angle ranging from 0° to 6° with 1.5° increment. From Fig. 15 it was observed that the ultimate buckling load and the initial stiffness reduced by 11.4% and 29.1%, respectively, when α = 6° compared to the pristine model with α = 0°. Even though it was observed to have significant effect on both the stiffness and ultimate buckling load, however, the post-buckled residual stiffness remained almost the same when the tilting angle varied.

The effect of the cross sectional and tow waviness defects was also studied. Non-linear post-buckling analysis was also performed considering models with different imperfections separately and combined. Fig. 16 shows predicted numerical result with different types of imperfections considered separately and combined compared with the baseline model result. Here the baseline model refers to a model with averaged cross-sectional dimension and 3° specimen tilting. As can be seen

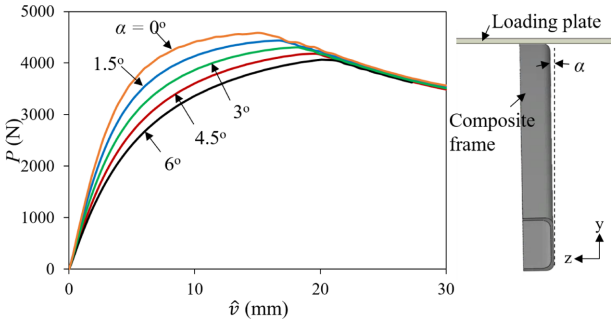

Fig. 14. Effect of tilting on post-buckling behavior

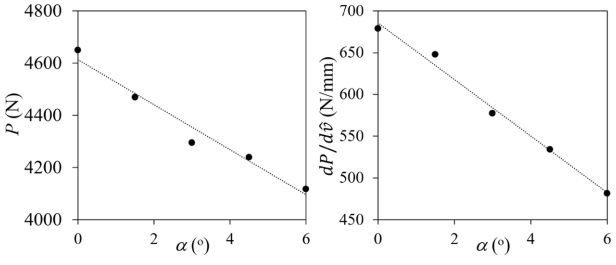

Fig. 15. Effect of tilting on ultimate buckling load (left) and initial stiffness (right)

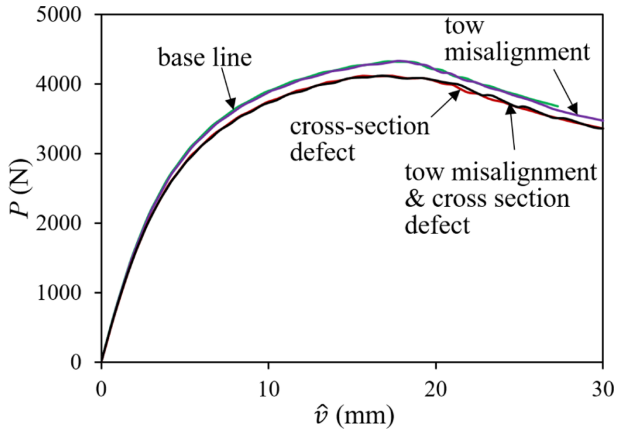

Fig. 16. Load-displacement curves for defects and uncertainties

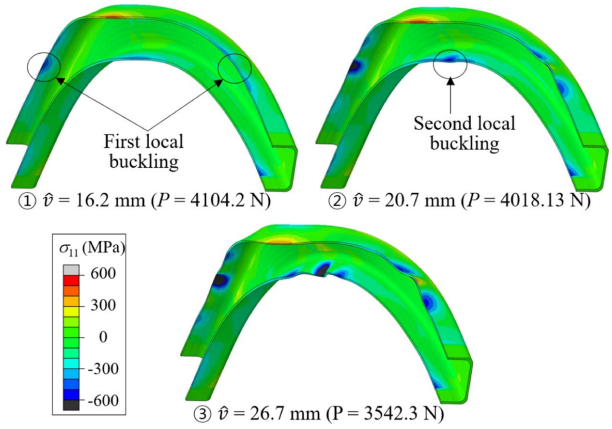

Fig. 18. Nonlinear buckling history with all defects considered

from the curves, the manufacturing defect in the form of longitudinal tow waviness had very small effect. The ultimate buckling load decreased by only 0.2%. In contrast, the buckling load with the cross-sectional defect reduced by 4.8%. In addition to the buckling load and stiffness reduction from cross-sectional defect, different buckling order was also resulted in which is described in the next section.

4.4 Comparison of test and analysis results

Fig. 17 compares the experimental load-displacement curve with the numerical prediction considering all defects. Both results showed a good correlation with the general trend matched. The predicted ultimate buckling load differs only by 2.3% compared to that by experiment.

Compared to the buckling behavior of the pristine model, a different buckling development behavior was observed due to the inclusion of defects. Fig. 18 shows the buckling deformation at three different loading stages corresponding to points indicated by the circled numbers in the load-displacement curve. As the applied displacement increase, the specimen initially showed the global bending out-of-plane deformation

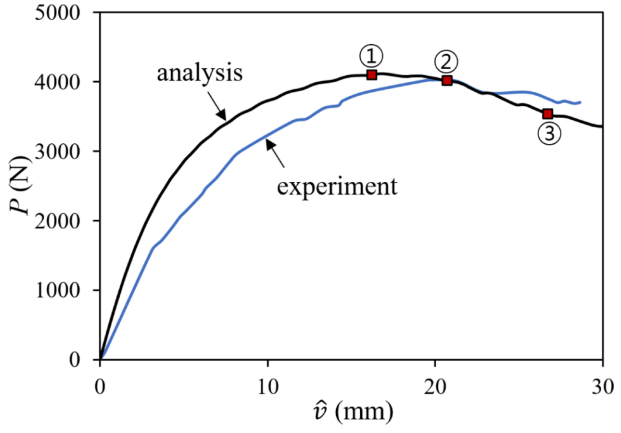

Fig. 17. Comparison of predicted and test load-displacement curves

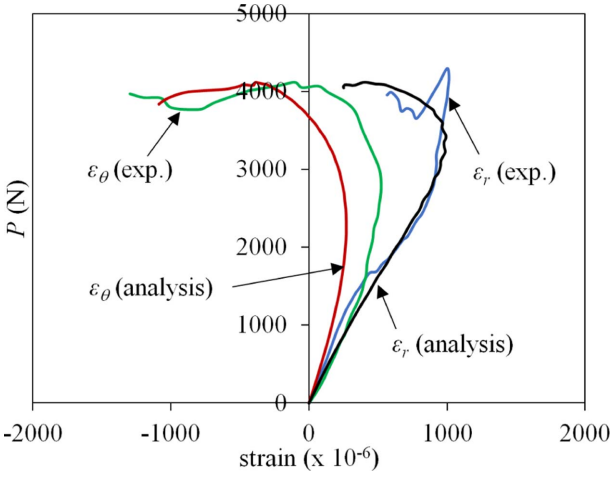

Fig. 19. Comparison of predicted and test load-strain curves

(mode 1). Then, when the displacement loading increased to 16.2 mm, local buckling started to develop at the upper flange between the support and the crown, which was different from the pristine model where the first local buckling appeared at the bottom flange of the crown part. Further increasing the displacement to 20.7 mm, the second local buckling developed at the bottom flange of the crown. After that, as the displacement increased the buckling deformation at the side and at the crown grew higher order buckling modes developing multiple waves.

The local deformation response from the strain gauges attached at the center of the web midway between the supports in radial (ε_r) and circumferential (ε_θ) direction was compared in Fig. 19. A good qualitative correlation was obtained for both directional strain readings despite the dependence of local reading to the presence of defect at that location.

5. CONCLUSIONS

In this paper, the buckling behavior of triaxially braided

composite arch frame under three-point bending was investigated using experimental and numerical approach. The manufacturing defects and uncertainty during test setup were identified and their effect on the buckling performance of the specimen was studied numerically. The predicted results were compared with the experimental results for verification. It was found that the global first bending mode of the composite circular arch was predicted to occur at the vertical load of 4771.4 N by linear buckling analysis, however it started develop from the beginning in geometrically nonlinear post-buckling analysis. In the geometrically nonlinear post-buckling analysis, the ultimate buckling load occurred when the first local buckling mode developed, indicating although the global buckling behavior depended on the global stiffness of the composite circular arch, the ultimate buckling load depended on the development of local buckling on top and bottom flange. It was also found that the manufacturing defect in the form of irregular cross section and imperfect test setup had significant effects on both linear buckling and geometrically nonlinear post-buckling behavior, while local tow misalignments had only minor effects. It was thought that the manufacturing quality should be tightly controlled to avoid defects in the composite specimen that could result in reduction in buckling loads and mode shape change.

ACKNOWLEDGEMENT

This work was supported by Defense Acquisition Program of Korea through Dual Use Technology Development Project 2018.

REFERENCES

1. Li, X., Binienda, W.K., and Goldberg, R.K., "Finite-element Model for Failure Study of Two-dimensional Triaxially Braided Composite," *Journal of Aerospace Engineering*, Vol. 24, No. 2, 2010, pp. 170-180.
2. Xu, L., Kim, S.J., Ong, C.H., and Ha, S.K., "Prediction of Material Properties of Biaxial and Triaxial Braided Textile Composites," *Journal of Composite Materials*, Vol. 46, No. 18, 2012, pp. 2255-2270.
3. Kosztowny, C.J., and Waas, A.M., "Buckling and Post-Buckling Behavior of Unitized, Stiffened Tri-Axially Braided Composite Textile Plates," Proceeding of the 55th SDM Conference, Maryland, Jan. 2014.
4. Potdar, S.A., and Bajad, M.N., "Design Method Prediction for Flexural Torsional Buckling Re-sistance of Steel Circular Arches-Box-Section", *Journal of Modern Engineering Research*, Vol. 6, Iss. 7, 2016, pp. 8-14.
5. Dou, C., Guo, Y.L., Zhao, S.Y., and Pi, Y.L., "Experimental Investigation into Flexural-torsional Ultimate Resistance of Steel Circular Arches," *Journal of Structural Engineering*, Vol. 141, No. 10, 2015, pp. 1-12.
6. Guo, Y.L., Zhao, S.Y., Pi, Y.L., Bradford, M.A., and Dou, C., "An Experimental Study on Out-of-plane Inelastic Buckling Strength of Fixed Steel Arches," *Engineering Structures*, Vol. 98, 2015, pp. 118-127.
7. Barbero, E., and Tomblin, J., "Euler Buckling of Thin-walled Composite Columns," *Thin-walled Structures*, Vol. 17, No. 4, 1993, pp. 237-258.
8. Qiao, P., Zou, G., and Davalos, J.F., "Flexural–torsional Buckling of Fiber-reinforced Plastic Composite Cantilever I-beams," *Composite Structures*, Vol. 60, No. 2, 2003, pp. 205-217.
9. Omidvar, B., and Ghorbanpoor, A., "Nonlinear FE Solution for Thin-walled Open-section Composite Beams," *Journal of Structural Engineering*, Vol. 122, No. 11, 1996, pp. 1369-1378.
10. ASTM E1856-13, "Standard Guide for Evaluating Computerized Data Acquisition Systems Used to Acquire Data from Universal Testing Machines," ASTM International, West Conshohocken, PA, 2013.
11. Hassan, N.K., and Mosallam, A.S., "Buckling and Ultimate Failure of Thin-walled Pultruded Composite Columns," *Polymers and Polymer Composites*, Vol. 12, No. 6, 2004, pp. 469-481.
12. Lee, J.H., and Kim, S.E., "Flexural–torsional Buckling of Thin-walled I-section Composites," *Computers & Structures*, Vol. 79, No. 10, 2001, pp. 987-995.
13. Arbelo, M.A., Kalnins, K., Ozolins, O., Skukis, E., Castro, S.G.P., and Degenhardt, R., "Experimental and Numerical Estimation of Buckling Load on Unstiffened Cylindrical Shells Using a Vibration Correlation Technique," *Thin-Walled Structures*, Vol. 94, 2015, pp. 273-279.
14. Hosseini-Toudeshky, H., Hosseini, S., and Mohammadi, B., "Delamination Buckling Growth in Laminated Composites Using Layerwise-interface Element," *Composite Structures*, Vol. 92, No. 8, 2010, pp. 1846-1856.
15. Schenk, C.A., and Schuëller, G.I., "Buckling Analysis of Cylindrical Shells with Random Geometric Imperfections," *International Journal of Non-Linear Mechanics*, Vol. 38, No. 7, 2003, pp. 1119-1132.
16. Sadovský, Z., Kriváček, J., Ivančo, V., and Ďuricová, A., "Computational Modelling of Geometric Imperfections and Buckling Strength of Cold-formed Steel," *Journal of Constructional Steel Research*, Vol. 78, 2012, pp. 1-7.
17. Mekonnen, A.A., and Woo, K., "Effects of Defects on Effective Material Properties of Triaxially Braided Textile Composite", Submitted to *International Journal of Aeronautical and Space Sciences*, 2019.
18. ASTM D3039/D3039M-17, "Standard Test Method for Tensile Properties of Polymer Matrix Composite Materials," ASTM International, West Conshohocken, PA, 2017.
19. Alpha STAR Corporation, *MCQ-Composites Theoretical Manual*, Alpha STAR Corporation, 2014.
20. Geleta, T.N., Woo, K.S., and Lee, B.H., "Prediction of Effective Material Properties for Triaxially Braided Textile Composite," *International Journal of Aeronautical and Space Sciences*, Vol. 18, No. 2, 2017, pp. 222-235.